

Atomic structure of the (111) surface of the antiferromagnetic 1/1 Au-Al-Tb approximantSam Coates *Department of Materials Science and Technology, Tokyo University of Science, 6 Chome-3-1 Nijuku, Katsushika City, Tokyo 125-8585, Japan*


Kazuki Nozawa

Department of Physics and Astronomy, Kagoshima University 1-21-35, Korimoto, Kagoshima 890-0065, Japan

Masahiro Fukami and Kazuki Inagaki

Department of Materials Science and Technology, Tokyo University of Science, 6 Chome-3-1 Nijuku, Katsushika City, Tokyo 125-8585, Japan

Masahiko Shimoda

*National Institute of Materials Science, Research Center for Advanced Measurement, 1-2-1 Sengen, Tsukuba, Ibaraki 305-0047, Japan*Ronan McGrath and Hem Raj Sharma *Surface Science Research Centre and Department of Physics, University of Liverpool, Liverpool L69 3BX, United Kingdom*Ryuji Tamura *Department of Materials Science and Technology, Tokyo University of Science, 6 Chome-3-1 Nijuku, Katsushika City, Tokyo 125-8585, Japan*

(Received 4 August 2020; accepted 2 December 2020; published 15 December 2020)

The recently discovered antiferromagnetic 1/1 Au-Al-Tb approximant exhibits a whirling spin order oriented along the [111] direction. Here we report an investigation of the atomic structure of the (111) surface by scanning tunneling microscopy and density functional theory (DFT) calculations. Scanning tunneling microscopy reveals a Tb-terminated step-terrace morphology, with step heights appearing to minimize the number of broken bulk icosahedra. The atomic structure of the terraces is bias dependent, with Tb atoms imaged under positive bias and Au/Al atoms under negative bias. The surface is found to reconstruct, with the Au/Al atoms producing a linear row structure, an example of a surface reconstruction in a Tsai-type system. These observations are confirmed by DFT calculations.

DOI: [10.1103/PhysRevB.102.235419](https://doi.org/10.1103/PhysRevB.102.235419)**I. INTRODUCTION**

A potential route to discovering long-range magnetic order in quasicrystals lies in the stoichiometric manipulation of their periodic analogs, or approximants. Recent reports detail how composition can affect the type of magnetic order in Au-based approximants, with antiferromagnetic order evident in approximants of increasing complexity [1–3]. These approximants belong to a family of complex intermetallics known as Tsai types, so called for their building block in the bulk, the Tsai-type cluster [4]. As Tsai-type approximants and quasicrystals share this same essential component, it is hoped that further manipulation may result in the synthesis of quasicrystal with long-range magnetic order.

The Tsai-type cluster is formed by a system of five hierarchical shells as shown in Fig. 1(a), where a tetrahedron (gray) is enclosed by a dodecahedron (yellow), icosahedron (green), icosidodecahedron (blue), and finally a rhombic triacontahedron (red). In this scheme, rare-earth (RE) atoms solely occupy the vertices of the icosahedron shell [green in Fig. 1(a)], while the other atoms occupy the vertices of the remaining shells (and the midedge points of the fifth shell

[4,5]. In quasicrystals, these clusters are distributed quasiperiodically, while in approximants they decorate the lattice points of the crystal structure. The understanding of the structure of Tsai-type materials allows for in-depth interpretations of phase-specific and stoichiometric-specific properties, including magnetic transitions [2,2,3,6], novel electronic properties [7–9], and superconductivity [10–12].

For example, it has been reported recently that the spin structure of the antiferromagnetic 1/1 Au-Al-Tb approximant can be described by the spin vectors of Tb atoms of individual icosahedra. Each spin vector is rotated approximately 86° with respect to the positional vector which describes the atomic position, relative to the center of each icosahedron [13]. Icosahedra at the body center and origin exhibit opposite spins, hence producing long-range antiferromagnetic order. The resultant magnetic structure can be described as a whirling spin order along the [111] direction. Figure 1(b) demonstrates an orthographic view of the [111] direction, showing origin and body-center icosahedra, with spin vectors shown in blue and red, respectively. Equivalent positions on the icosahedra exhibit opposite spin.

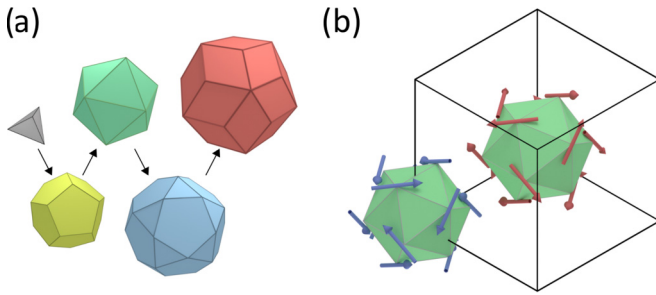


FIG. 1. (a) Tsai-cluster model of hierarchical shells. A tetrahedron (gray) is contained within a dodecahedron (yellow), icosahedron (green), icosidodecahedron (blue), and rhombic triacontahedron (red). (b) Orthographic projection along the $[111]$ direction of the $1/1$ Au-Al-Tb unit cell, showing the spins of the origin and body-center icosahedra.

It is therefore of obvious interest to characterize the magnetic properties of the (111) surface. As a starting point, we investigate the atomic structure of the (111) surface. This will allow for an understanding of the magnetic surface structure and also presents an opportunity to study a hitherto unreported surface of a Tsai-type approximant. In general, approximants have received comparatively less attention [14–16] than the high-symmetry surfaces of Tsai-type quasicrystals, which have been extensively studied, with considerable effort made to understand both surface structure and surface chemistry [17–29].

We find that the surface (111) surface of $1/1$ Au-Al-Tb terminates at bulk planes containing Tb atoms. In addition, the step-terrace structure is determined by the minimization of the number of truncated Tsai-cluster icosahedra. Furthermore, we show that the Au/Al atoms of the surface form a rowlike reconstruction, an example of such a phenomenon at a Tsai-type material surface.

II. METHODS

High-purity Au ($4N$), Al ($4N$), and Tb ($3N$) raw materials of the nominal composition $\text{Au}_{71}\text{Al}_{19}\text{Tb}_{10}$ are melted at 1273 K for 3 h inside an alumina crucible under vacuum. Single grains are prepared using the self-flux method and the specimen is slowly cooled to 1003 K at a rate of 3 K/min. Single grains are separated from the molten flux using a centrifuge. The characterization of single grains is performed by x-ray diffraction on pulverized powder. The x-ray-diffraction pattern shows that the obtained single grains are single $1/1$ approximant phases with $a = 1.47581$ nm. From the relationship between the lattice parameter and the composition, obtained for the polygrain $1/1$ Au-Al-Tb approximants, the composition of the single grains is estimated to be $\text{Au}_{70}\text{Al}_{16}\text{Tb}_{14}$, which falls inside the antiferromagnetic region. The magnetic susceptibility χ of single grains is measured in the temperature range between 2 and 300 K using a magnetic property measurement system (Quantum Design). A sharp cusp in χ - T due to an antiferromagnetic transition is observed at the Néel temperature $T_N = 11.9$ K. Thus, antiferromagnetic single grains with $T_N = 11.9$ K are successfully obtained in the present work.

The (111) surface of a single crystal of $1/1$ Au-Al-Tb is polished with successively finer grades of diamond paste (from 6 to $0.25 \mu\text{m}$) before washing in methanol. The surface is then further cleaned with sputter-anneal cycles (30-min Ar^+ sputter and 2-h anneal at 730 K) under ultrahigh-vacuum conditions. Substrate cleanliness is monitored with room-temperature scanning tunneling microscopy (STM). Using x-ray spectroscopy, it is found that after sputtering Al is preferentially removed from the surface, being the lightest element. However, a bulklike starting composition is restored after the annealing process, indicating that no phase change has occurred. A similar phenomenon was observed in Al-based quasicrystals [30]. As this is above T_N , the sample is in a paramagnetic phase. Bias conditions are referred to with respect to the STM tip, so positive bias images unoccupied states and vice versa.

Calculations on the surface structure are based on density functional theory using the plane-wave basis set implemented in the Vienna Ab initio Simulation Package [31]. The electron-ion interactions are described by the projector augmented-wave potentials [32] with the exchange-correlation functional in the generalized gradient approximation proposed by Perdew *et al.* [33]. The localized $4f$ electrons of Tb are kept frozen in the core. The basis set contains plane waves with a kinetic energy up to 240 eV. We perform non-spin-polarized calculations, since no significant difference in the surface atomic structure is observed in the spin-polarized calculations carried out for comparison. The surface is approximated by a repeated slab model composed of an atomic layer of about 0.8 nm and vacuum layer of over 1.2 nm. The Brillouin zone is sampled by a $1 \times 5 \times 5$ Monkhorst-Pack grid yielding 13 irreducible k points. The atomic positions are optimized using the calculated Hellmann-Feynman forces and conjugate gradient method excepting the atoms located at the bottom of the atomic layer assumed as the bulk. The convergence criteria of 10^{-5} and 10^{-4} eV are applied for the electronic and ionic loops, respectively. Simulated STM images are calculated within the Tersoff-Hamann approximation [34].

III. RESULTS AND DISCUSSION

A. Step morphology

Figure 2(a) shows a large-scale STM image of the surface, where a step-terrace morphology is observed. A terrace kink angle α is marked, with a value of $119^\circ \pm 2^\circ$, consistent with threefold symmetry expected from the bulk model structure. Figure 2(b) shows a histogram taken from Fig. 2(a), illustrating the distribution of step heights, with the most common step height measured as 1.22 ± 0.04 nm. Islandlike protrusions are regularly observed on top of the terraces, with examples circled in white. The heights of these islands are between 0.3 and 0.4 nm, with no defined morphology evident. The width of individual terraces rarely exceeds 100 nm, independent of annealing conditions. The islands and small terrace size therefore suggests a low stability in comparison to, for example, the threefold surface of i -Ag-In-Yb (the quasicrystalline analog), which produces flat terraces with widths upward of 300 nm.

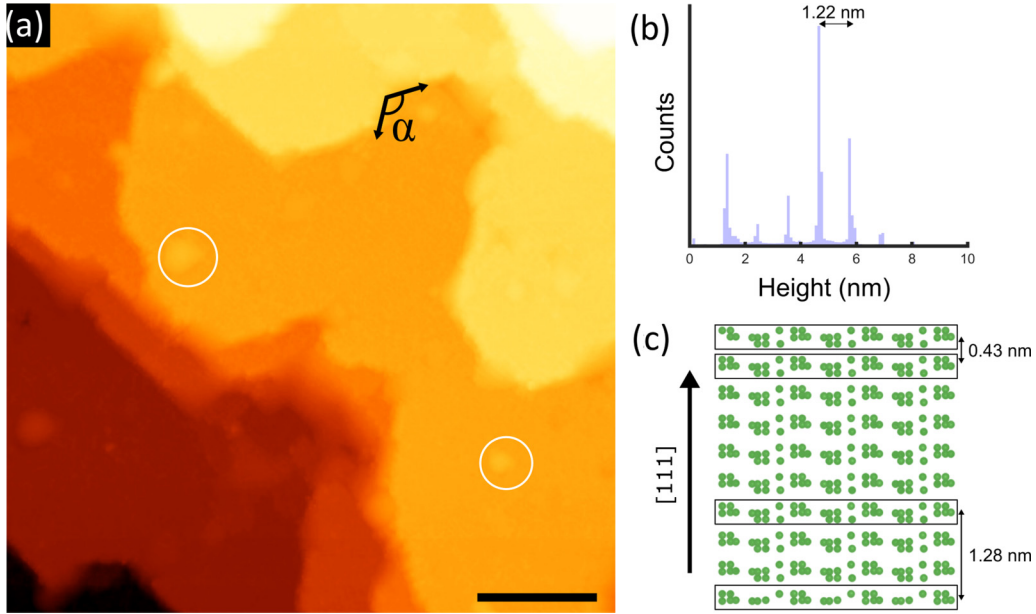


FIG. 2. (a) STM image ($V_b = 2$ V and $I_t = 172$ pA) of the step terrace structure of the (111) surface. Here α indicates the terrace kink angle. White circles mark islands. The scale bar is 30 nm. (b) Histogram taken from (a), showing the step height distribution. The average step height is labeled. (c) Bulk model of Tb planes arranged along the [111] direction. Groups of three planes are separated by 0.43 nm, as labeled. Groups of planes which correspond to the measured step height are also indicated.

We consider the step heights in terms of planes of atoms in the bulk model. Figure 2(c) shows a side view of the Tb planes in the bulk, arranged perpendicular to the [111] direction. Three Tb planes form what we will refer to as Tb surface slabs, examples of which are bounded by black boxes. The separation of these slabs (i.e., center to center) is 0.43 nm. Therefore, the measured step height can be considered as the separation between four slabs, 1.28 nm, as indicated at the bottom of Fig. 2(c). It should be noted that this value and the measured step height (1.22 nm) are 1.5 times larger than the separation of adjacent lattice planes in the bulk $d = \frac{a}{\sqrt{h^2+k^2+l^2}} = 0.8521$ nm (where $a = 1.4758$ nm [2]). A possible explanation for the large step height will be discussed later.

Every Tsai-type quasicrystal surface studied by STM has been found to be rare-earth-atom terminated, that is, the surface planes are densely populated by rare-earth atoms [18,19,23]. This has been linked to both the low surface free energy and low-lying unoccupied 3d states of the rare-earth (RE) atoms which act to stabilize the surface [23,35,36]. Despite a lack of atomic resolution on the Ag-In-R(100) approximant surfaces ($R = \text{Yb, Tb, and Gd}$), it was regarded as likely that it is also true for these cases [16]. Therefore, the step heights for the (111)Au-Al-Tb surface are considered in terms of Tb dense planes.

B. Atomic structure

1. Positive bias and spin structure

The structure of the surface can be resolved with subcluster (but not atomic) resolution. First, we consider positive-bias images [Figs. 3(a) and 3(b)]. Figure 3(a) shows a set of dimer-like bright protrusions which are arranged in a rhombohedral surface unit cell with lattice parameters $a = 2.12 \pm 0.07$ nm,

$b = 2.10 \pm 0.04$ nm, and $\alpha = 58^\circ \pm 2^\circ$ where the marked vectors intersect the center point of the dimers. An example of adjacent protrusions (separated by 1.23 ± 0.03 nm) in the dimers is highlighted by an oval. The dimers can also be considered as forming hexagons enclosing an area of dark contrast, highlighted by the black hexagon.

Figure 3(b) shows a different area of the surface observed at the same bias value as in Fig. 3(a). The apparent change in morphology, where the dark centers of the hexagons in Fig. 3(a) are resolved as low-intensity protrusions, may arise from a change in tip/tunneling conditions. A rhombohedral cell which includes the below-plane protrusion in the hexagon has the parameters $c = 1.23 \pm 0.07$ nm, $d = 1.24 \pm 0.08$ nm, and $\beta = 61^\circ \pm 2^\circ$.

In previous work on Tsai-type quasicrystal and approximant surfaces, rare-earth atoms were detected under positive-bias conditions [18,19,23,29]. Therefore, we consider similar behavior in our analysis. As previously discussed, the Tb slabs used to explain the step heights consist of three closely separated Tb planes [Fig. 2(c)]. The structure observed in Fig. 3(a) can be understood using the center of these three planes. Figure 3(c) shows a model of this plane, which consists of sets of Tb atoms arranged in triangles with edge lengths 0.55 nm, rotated 60° with respect to each other. These triangles are canted with respect to the surface vectors by approximately 7° . The rhombohedral and hexagonal cells highlighted in Fig. 3(a) are also marked in Fig. 3(c), where each bright protrusion observed corresponds to an individual triangle. The model rhombohedral unit cell gives values of $a = b = 2.09$ nm, a good fit with the experimental value.

The alternative positive-bias structure observed in Fig. 3(b) can be explained by the tip tunneling to the lowest Tb plane in the slab. This plane consists of larger edge length Tb triangles (0.9 nm) with only one orientation and is shown in addition

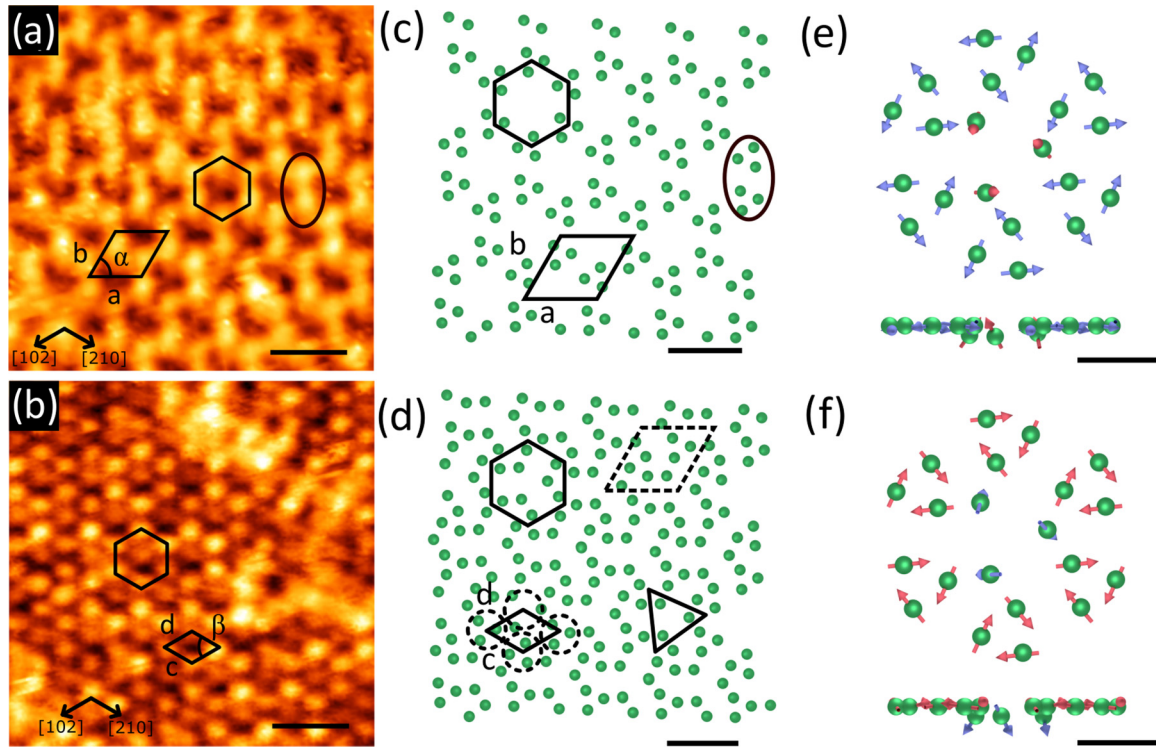


FIG. 3. (a) STM image ($V_b = 1900$ mV and $I_t = 175$ pA) showing the atomic structure of a terrace. Bright dimerlike protrusions (highlighted by an oval) form a rhombohedral unit cell or hexagonal structure, both marked. The crystallographic direction is marked. The scale bar is 3 nm. (b) STM image ($V_b = 1900$ mV and $I_t = 172$ pA) showing additional features which appear dependent on tip condition. Again rhombohedral and hexagonal cells are marked. The crystallographic direction is marked. The scale bar is 3 nm. (c) Model schematic of Tb atoms (green) forming the structure in (a). The corresponding features (oval, rhombohedron, and hexagon) are marked. The scale bar is 3 nm. (d) Model structure used to explain the additional feature in (b). The scale bar is 3 nm. (e) and (f) Resultant spin structures of the hexagon highlighted in (b) and (d) at two different terraces. Arrows denote the spin direction, while the color indicates the type of icosahedron responsible for the spin. Planar views are shown below. Scale bars are 1 nm.

to the middle Tb plane in Fig. 3(d), where examples of the larger triangles are highlighted. A dashed rhombohedron indicates the projected bulk unit cell. Dashed circles indicate the protrusions measured by STM. The addition of these triangles forms a small rhombohedral cell as highlighted, with dimensions commensurate with the experimental values $c = d = 1.21$ nm. As the structures observed in Figs. 3(a) and 3(b) can be explained using only the bottom two planes of a Tb slab, we infer that the surface terminates at the middle Tb plane. A possible explanation for this plane selection will be discussed later.

As the Tb atoms carry the magnetic order of the sample, we can visualize the resultant spin structure of the two surface Tb planes below T_N using the previously described structure taken from [13]. We can also consider the magnetic structure as two interpenetrating simple cubic lattices, each of which is decorated by one type of spin icosahedron [i.e., one of the two icosahedra in Fig. 1(b)]. We will broadly describe these as either up or down icosahedra to simply differentiate their spin structures.

Using the observed step height as a guide, we can truncate the bulk spin model at one of two terraces. These terraces exhibit opposing spins. Figures 3(e) and 3(f) show the spin structures of the hexagons highlighted in Figs. 3(b) and 3(d). Colored arrows denote spins from either an up icosahedron (blue) or a down icosahedron (red). The small triangles of the

top Tb plane are formed by up (down) icosahedra, while the larger triangles of the Tb plane below are formed by down (up) icosahedra. Adjacent small triangles show sets of spins rotated by 60° . As the spin vectors are canted with respect to their position vectors, the spins are not exactly parallel/perpendicular with the surface direction, as indicated by the planar views at the bottom of Figs. 3(e) and 3(f).

2. Negative bias and reconstruction

Figures 4(a) shows the surface as imaged with negative bias, where a bright row structure with overall twofold symmetry is observed. We note that this surface morphology is observed for a range of bias conditions (i.e., from -2000 to approximately 1000 mV). Swapping between large bias polarities in the same area of the sample (i.e., from -1900 to 1900 mV) confirms that this row morphology is not an impurity phase, i.e., it is possible to reproduce the structure in Figs. 3(a) and 3(b) simply by switching to a high positive bias. Likewise, the row directions are independent of scanning direction or tip condition, as confirmed by rotating the scan orientation and undertaking multiple tip-cleaning procedures. Therefore, we consider this morphology as a result of a surface reconstruction.

The distance between adjacent rows is 1.06 ± 0.09 nm. A V-shaped protrusion is highlighted by a black circle,

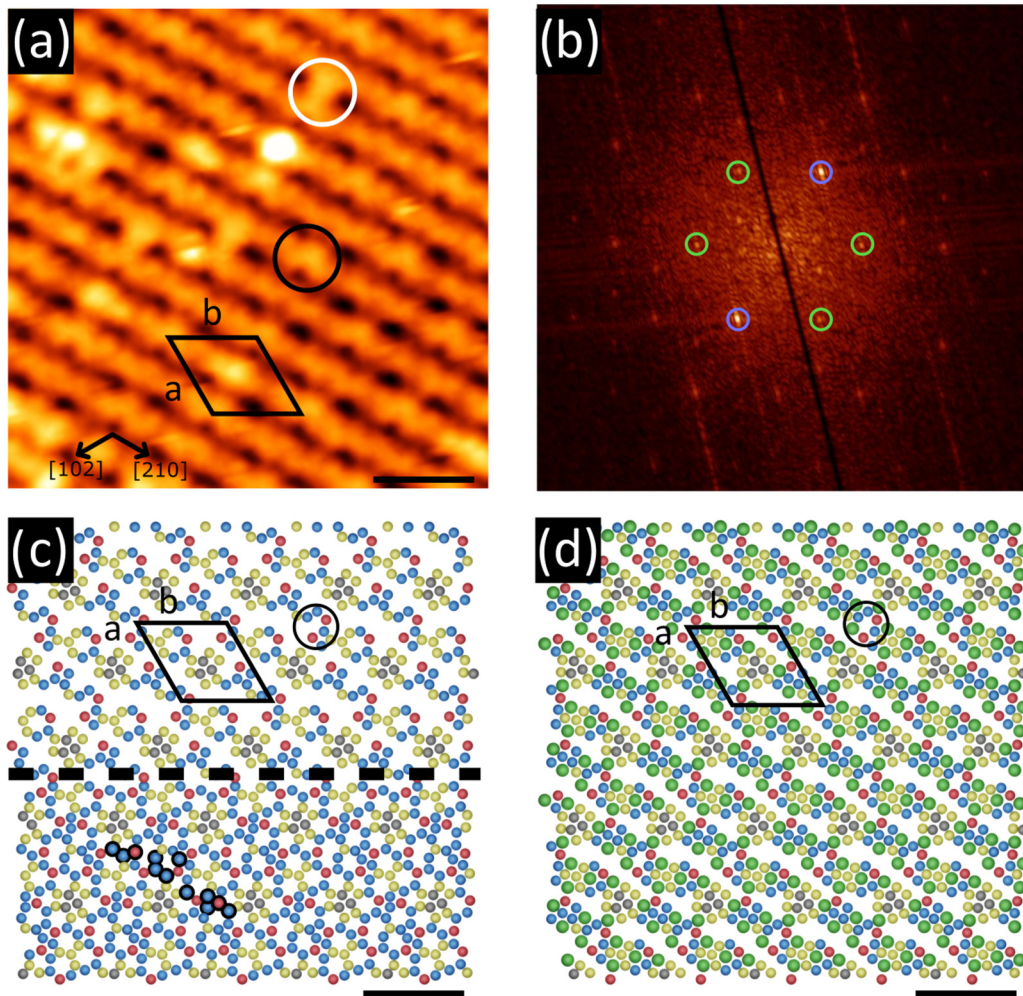


FIG. 4. (a) STM image ($V_b = -1000$ mV and $I_t = 140$ pA) of the terrace morphology under negative bias. A rhombohedral unit cell is marked, linking V-shaped protrusions, one of which is circled in black. The crystallographic direction is marked. The scale bar is 3 nm. (b) FFT of (a), where spots are highlighted by circles, showing the sixfold symmetry of the distribution of the V-shaped protrusions. The blue circles mark spots of increased intensity, indicating the twofold symmetry of the rows. (c) Model schematic of (a). Red, blue, yellow, and gray circles indicate fifth-, fourth-, second-, and first-shell positions of Au/Al atoms. The bulk truncated model is shown below the dashed line. A set of individual atoms is circled, indicating which atoms are removed under the reconstruction. Above the dashed line, the rhombohedral unit cell and V-shaped protrusions of (a) are marked. The scale bar is 3 nm. (d) Model slab of the surface including Tb atoms. The rhombohedral unit cell and V-shaped protrusions of (a) are again marked. The scale bar is 3 nm.

which forms a marked rhombohedral unit cell between the bright rows, with the parameters $a = 2.09 \pm 0.06$ nm and $b = 2.15 \pm 0.04$ nm, i.e., the same unit cell dimensions as in Fig. 4(c). Inside the marked unit cell is a section of a bright row. Occasionally a feature will bridge between two rows: An example is circled in white, which will be discussed later. A fast Fourier transform (FFT) of Fig. 4(a) is shown in Fig. 4(b) to demonstrate the symmetry of the morphology observed. Here the expected sixfold symmetry from a (111) surface termination is shown by the set of spots highlighted by the colored circles, which are arranged in a hexagon. However, the intensity of the spots varies, as made evident by comparing those circled in blue to those circled in green. The brighter spots reflect the twofold nature of the rows, while the entire set of spots indicates that there is a threefold symmetric network embedded within the row structure, i.e., the V-shaped protrusions.

We analyze the observed structure using Au/Al atoms contained within the surface slab used to explain Figs. 3(a) and 3(b). As a twofold row structure cannot be obtained by a simple bulk truncation, we instead consider a missing-row structure in which several atoms of the unit cell in the topmost plane are removed. It is presumed that these atoms desorb, are incorporated at step edges via diffusion during the cleaning process, or are perhaps visible as the bright island-type defects highlighted in Fig. 2(a).

Figure 4(c) shows the surface model considering all non-Tb positions. Here the atoms of each shell are represented as spheres and are colored as in Fig. 1(a). The bulk-truncated model is shown below the dashed line. A set of 12 atoms is highlighted by black circles, representing the atoms which are removed from the surface unit cell to obtain the surface reconstruction. The choice of these atoms was determined by a trial-and-error comparison between experimental and

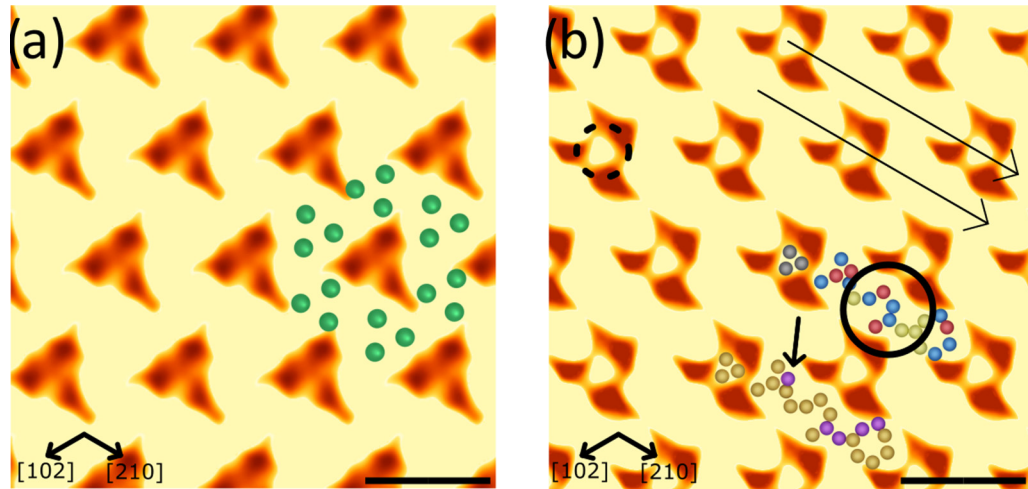


FIG. 5. (a) Simulated STM image at $V_b = +1900$ mV. Bright circles form a hexagonal network matching the STM image of Fig. 3(a). Overlaid are some of the Tb atoms which form the hexagonal structure. A dim triangle can be seen at the center of the hexagon, i.e., from the lower Tb plane in Fig. 3(d). The scale bar is 2 nm. (b) Simulated STM image at $V_b = -1900$ mV. The row structure as observed in Fig. 4(a) can be clearly seen and is indicated by two parallel arrows. Overlaid are sections of the reconstructed model: One section is colored as with the Tsai-type shells and the other is colored to represent its chemistry, i.e., Au is gold and Al is purple. The V-shaped protrusion and bridging feature in Fig. 4(a) are indicated with a black circle and an arrow, respectively. A dashed circle indicates a protrusion from first-shell atoms. The scale bar is 2 nm.

simulated STM images, which are discussed later. Above the dashed unit cell is the proposed reconstruction. The separation between adjacent rows is approximately 1.05 nm, matching the experimentally observed value. A group of atoms is highlighted by a black circle, indicating the proposed origin of the V-shaped protrusion. The marked unit cell joins four of these groups together, with $a = b = 2.09$ nm, again fitting with the experimental values. Likewise, inside the unit cell is a row of atoms which corresponds to the row inside the cell of Fig. 4(a). The overall surface structure is therefore presented in Fig. 4(d), composed of a threefold network of Tb triangles within a twofold row structure of Au/Al atoms. The unit cell and V-shaped protrusion from Fig. 4(c) are overlaid for comparison.

3. Simulated STM

To confirm the comparison between the model and the experimentally observed structure, STM images are simulated using a range of different surface models. Models are changed by removing different sets of Au/Al atoms from the unit cell, in addition to changing the chemistry of the atoms of the surface (i.e., switching between Au and Al at sites with nearly equivalent partial occupancy [2]). Before calculating the STM isosurface, each model is structurally relaxed and subsequent desorption energies are calculated. Often, the relaxations lead to unstable Au/Al atoms and qualitatively ill-fitting models. Occasionally, Tb atoms are also shifted, leading to poor fits across all bias conditions. Calculations are performed with different Tb terminations, i.e., either with all three Tb planes from the surface slab of Fig. 2(c) or with the bottom two as shown in Figs. 3(d) and 4(d).

The model which produces the best fit, with no unstable surface atoms, is that shown in Fig. 4(d). After a structural relaxation of this model, the isosurfaces for positive and neg-

ative bias are calculated. Figure 5(a) shows the result of the simulation for positive bias (+1900 mV). Bright protrusions match the dimerlike network observed in Fig. 3(a). Overlaid is a series of Tb atoms, so that each protrusion of a hexagon is formed by a Tb triangle. The center of the hexagon is dark, although a dim triangle can be seen. This corresponds to the larger Tb triangle of the lower Tb plane, as previously mentioned when discussing Fig. 3(b).

Figure 5(b) shows the surface model as simulated under negative bias (-1900 mV). The structure observed matches that seen in Fig. 4(a), i.e., rhombohedral overall, yet with a row structure. The rows are indicated by two long arrows. Overlaid on top of a section of a row, colored as the Tsai cluster shells in Fig. 1(a), are the Au/Al atoms which contribute to the observed local density of states (LDOS). A black circle indicates the group of atoms which forms the V-shaped protrusion in Fig. 4(a). A dashed circle indicates a bright protrusion which appears separated from other LDOS contributions. According to the surface model, it is produced by atoms belonging to the first shell [i.e., the tetrahedron in Fig. 1(a)] of the Tsai cluster. Typically, this shell is not considered in surface studies of Tsai-type materials, as its dynamics leads to an ill-defined surface contribution [37–39]. To represent the tetrahedron, we have assumed four Au atoms occupy nonadjacent vertices of a small cube, similar to the cubic unit cell of the bulk. There are two possible orientations of the tetrahedron, up and down, where one of the Au atoms occupies the (111) and $(-1, -1, -1)$ vertices of the cube, respectively. Changing the relative orientations of the tetrahedra has little to no effect on the calculated STM image, so we arbitrarily assign them as up tetrahedra.

Overlaid in Fig. 5(b) is a second set of atoms which are colored to represent their chemistry, so that Au atoms are gold and Al atoms are purple. The bridging protrusion highlighted in white in Fig. 4(a) is indicated by an arrow. As this feature

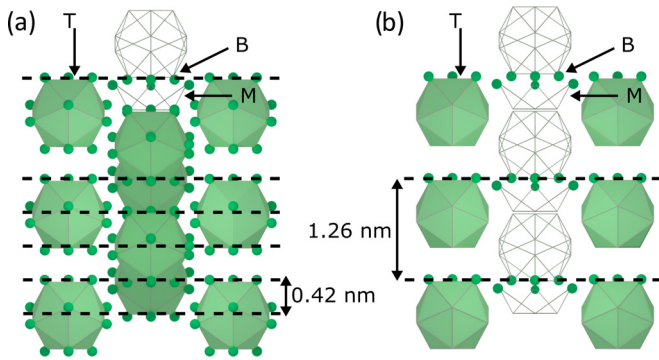


FIG. 6. (a) Bulk model of Tb atoms illustrating where surface terminations would truncate the Tb icosahedra, either at the top (T), bottom (B), or middle (M). Skeletal structures highlight the nature of the truncation. Dashed lines separated by 0.43 nm illustrate the minimum step height for Tb atoms. (b) Same schematic as (a), altered to reflect the measured step height. The visible planes of Tb atoms are those in Fig. 3(d).

is only occasionally seen by STM, it is presumed either that atoms at or near this position are partially removed during cleaning or that the chemistry of the site changes (due to partial occupancy [2]) so that the LDOS contribution also changes.

4. Surface stability

Here we discuss the surface truncation and stability in comparison to quasicrystalline surfaces. The (111) surface of Au-Al-Tb is a periodic analog to the threefold surface of a Tsai-type quasicrystal. On the threefold surface of *i*-Ag-In-Yb, terraces are formed at every so-called cluster-center plane [19]. These are dense planes which contain the geometric centers of the Tsai clusters which form the bulk structure of the quasicrystal. These planes invariably produce a high density of RE atoms. As previously discussed, the stability of the surface termination has been linked to the RE atoms [19,23,35,36].

The periodic interpretation of cluster-center planes for the Au-Al-Tb(111) system would simply be the lattice points of the body-centered-cubic structure. If Au-Al-Tb(111) were to be terminated at every cluster-center plane, as with the quasicrystal, we would see step heights at every 0.43 nm ($0.5 \times d$), as demonstrated by the Tb slabs in Fig. 2(c). If this were the case, adjacent terraces would display the same structure with a relative shift of $\sqrt{2}a$. Instead, we see separations of $1.5 \times d$. Again, the structures of adjacent terraces are identical except for the $\sqrt{2}a$ shift. Both geometrically and chemically, therefore, there is no difference between step heights of 0.5 and $1.5 \times d$. The selection of larger step heights suggests that there is another driving force for these step heights beyond the terrace constituents and their arrangement.

Figure 6(a) shows a section of the Tb atoms of the bulk structure along the [111] direction, i.e., an enlarged version of Fig. 2(c). Here the icosahedral shells which are used to model the atoms are included. Dashed black lines show prospective truncations at every cluster-center plane, i.e., step heights of 0.43 nm. At the top of Fig. 6(a) three icosahedra

are marked by letters, indicating the positions on the icosahedra through which the plane of truncation intersects. For instance, the icosahedron labeled as the top (T) will donate its top atoms to the surface plane. The middle icosahedron (M) is broken just below its midpoint, while the bottom (B) donates its bottom atoms. The top and bottom truncations both provide triangles of edge length 0.55 nm, i.e., the bright protrusions in Figs. 3(a) and 5(a). The middle icosahedron gives the larger Tb triangles in the lower plane, as described in Fig. 3(d).

The icosahedra can also be considered in terms of how broken they are, i.e., full (top), half full (middle), or empty (bottom), as indicated by the skeletal structures in Fig. 6(a). It follows that truncations at every 0.43 nm would produce the maximum number of broken icosahedra: If we study one icosahedron in Fig. 6(a), we see that it could be truncated three times. Figure 6(b) is an alternate version of Fig. 6(a), which shows only the icosahedra involved in bulk truncations at every 1.28 nm, the experimentally observed step height. Some atoms have also been removed for clarity; the remaining atoms are those detected by STM in Fig. 3. We suggest that this model shows a possible explanation for the enlarged step height, through the preservation of as many unbroken icosahedra as possible. To demonstrate, we calculate the number of whole icosahedra in a section of the bulk for each step height (i.e., 0.43 and 1.28 nm), for five step heights. To do so, we build a quasi-two-dimensional slice with one unit cell thickness and five unit cells in width; the height of the slab is then determined by the step height value. Atoms are removed to simulate a step-terrace structure with five steps and the number of whole icosahedra is counted. The larger step height value gives 2.5 times as many unbroken icosahedra in the bulk. This behavior is contrary to the Tsai-type quasicrystalline system and may indicate that in this system, or along this crystallographic direction, the role of a full icosahedron has energetic implications as opposed to simply geometric. Such behavior has been previously observed on, for example, *i*-Al-Pd-Mn [40].

IV. CONCLUSION

We have investigated the (111) surface of the antiferromagnetic 1/1 Au-Al-Tb approximant, finding that the surface is terminated at Tb-containing planes, with a step height that appears to promote the minimization of broken icosahedra in the bulk. As Tsai-type quasicrystals do not appear to follow this scheme, this behavior could be investigated in the future on more complex Tsai-type approximants (i.e., 2/1), which contain all of the building blocks used to describe Tsai-type quasicrystals.

We have shown that there is a bias dependence in the terrace structure of the surface, where at positive bias we resolve Tb atoms arranged in a rhombohedral or hexagonal fashion. At negative bias we resolve Au/Al atoms, which are found to form the first reconstruction observed on a Tsai-type material surface. These observations are confirmed using density functional theory calculations. The unique mixture of twofold and threefold symmetric surface constituents will be an intriguing playground for studying epitaxy and molecular adsorption.

ACKNOWLEDGMENTS

This work was supported by Kakenhi Grants-in-Aid (Grants No. 19H05817 and No. 19H05818) from the Japan

Society for the Promotion of Science. The density functional theory calculations were done using the facilities of National Institute for Materials Science, Japan and the Institute for Solid State Physics, University of Tokyo.

- [1] A. Ishikawa, T. Hiroto, K. Tokiwa, T. Fujii, and R. Tamura, Composition-driven spin glass to ferromagnetic transition in the quasicrystal approximant Au-Al-Gd, *Phys. Rev. B* **93**, 024416 (2016).
- [2] A. Ishikawa, T. Fujii, T. Takeuchi, T. Yamada, Y. Matsushita, and R. Tamura, Antiferromagnetic order is possible in ternary quasicrystal approximants, *Phys. Rev. B* **98**, 220403(R) (2018).
- [3] S. Yoshida, S. Suzuki, T. Yamada, T. Fujii, A. Ishikawa, and R. Tamura, Antiferromagnetic order survives in the higher-order quasicrystal approximant, *Phys. Rev. B* **100**, 180409(R) (2019).
- [4] H. Takakura, C. P. Gómez, A. Yamamoto, M. de Boissieu, and A. P. Tsai, Atomic structure of the binary icosahedral Yb-Cd quasicrystal, *Nat. Mater.* **6**, 58 (2007).
- [5] A. P. Tsai, J. Q. Guo, E. Abe, H. Takakura, and T. J. Sato, Alloys: A stable binary quasicrystal, *Nature (London)* **408**, 537 (2000).
- [6] R. Tamura, Y. Muro, T. Hiroto, K. Nishimoto, and T. Takabatake, Long-range magnetic order in the quasicrystalline approximant Cd₆Tb, *Phys. Rev. B* **82**, 220201(R) (2010).
- [7] K. Deguchi, S. Matsukawa, N. K. Sato, T. Hattori, K. Ishida, H. Takakura, and T. Ishimasa, Quantum critical state in a magnetic quasicrystal, *Nat. Mat.* **11**, 1013 (2012).
- [8] T. Watanuki, S. Kashimoto, D. Kawana, T. Yamazaki, A. Machida, Y. Tanaka, and T. J. Sato, Intermediate-valence icosahedral Au-Al-Yb quasicrystal, *Phys. Rev. B* **86**, 094201 (2012).
- [9] S. Jazbec, S. Vrtnik, Z. Jagličić, S. Kashimoto, J. Ivkov, P. Popčević, A. Smontara, H. J. Kim, J. G. Kim, and J. Dolinšek, Electronic density of states and metastability of icosahedral Au-Al-Yb quasicrystal, *J. Alloys Compd.* **586**, 343 (2014).
- [10] K. Kamiya, T. Takeuchi, N. Kabeya, N. Wada, T. Ishimasa, A. Ochiai, K. Deguchi, K. Imura, and N. K. Sato, Discovery of superconductivity in quasicrystal, *Nat. Commun.* **9**, 1 (2018).
- [11] K. Deguchi, M. Nakayama, S. Matsukawa, K. Imura, K. Tanaka, T. Ishimasa, and N. K. Sato, Crystal structure of superconducting 1/1 cubic Au-Ge-Yb approximant with Tsai-type cluster, *J. Phys. Soc. Jpn.* **84**, 015002 (2015).
- [12] K. Deguchi, M. Nakayama, S. Matsukawa, K. Imura, K. Tanaka, T. Ishimasa, and N. K. Sato, Superconductivity of Au-Ge-Yb approximants with Tsai-type clusters, *J. Phys. Soc. Jpn.* **84**, 023705 (2015).
- [13] T. J. Sato, A. Ishikawa, A. Sakurai, M. Hattori, M. Avdeev, and R. Tamura, Whirling spin order in the quasicrystal approximant Au₇2Al₁4Tb₁4, *Phys. Rev. B* **100**, 054417 (2019).
- [14] S. Hars, H. Sharma, J. Smerdon, T. Yadav, R. Tamura, M. Shimoda, and R. McGrath, The structure of the (100) surface of Ag-In-Gd 1/1 approximant, *Acta Phys. Pol. A* **126**, 479 (2014).
- [15] C. Cui, H. Sharma, P. Nugent, M. Shimoda, and A. P. Tsai, STM study on the (100) surface of the Ag-In-Yb 1/1 cubic approximant, *Acta Phys. Pol. A* **126**, 577 (2014).
- [16] S. S. Hars, H. R. Sharma, J. A. Smerdon, T. P. Yadav, A. Al-Mahboob, J. Ledieu, V. Fournée, R. Tamura, and R. McGrath, Surface structure of the Ag-In-(rare earth) complex intermetallics, *Phys. Rev. B* **93**, 205428 (2016).
- [17] H. R. Sharma, M. Shimoda, S. Ohhashi, and A. P. Tsai, First UHV surface studies of single-grain icosahedral Ag-In-Yb quasicrystal, *Philos. Mag.* **87**, 2989 (2007).
- [18] H. R. Sharma, M. Shimoda, K. Sagisaka, H. Takakura, J. A. Smerdon, P. J. Nugent, R. McGrath, D. Fujita, S. Ohhashi, and A. P. Tsai, Structure of the fivefold surface of the Ag-In-Yb icosahedral quasicrystal, *Phys. Rev. B* **80**, 121401(R) (2009).
- [19] C. Cui, P. J. Nugent, M. Shimoda, J. Ledieu, V. Fournée, A. P. Tsai, R. McGrath, and H. R. Sharma, The atomic structure of the threefold surface of the icosahedral Ag-In-Yb quasicrystal, *J. Phys.: Condens. Matter* **24**, 445011 (2012).
- [20] P. J. Nugent, G. Simutis, V. R. Dhanak, R. McGrath, M. Shimoda, C. Cui, A. P. Tsai, and H. R. Sharma, Surface oxidation of the icosahedral Ag-In-Yb quasicrystal, *Phys. Rev. B* **82**, 014201 (2010).
- [21] P. J. Nugent, J. A. Smerdon, R. McGrath, M. Shimoda, C. Cui, A. P. Tsai, and H. R. Sharma, Step-terrace morphology and reactivity to C₆₀ of the five-fold icosahedral Ag-In-Yb quasicrystal, *Philos. Mag.* **91**, 2862 (2011).
- [22] H. R. Sharma, K. Nozawa, J. A. Smerdon, P. J. Nugent, I. McLeod, V. R. Dhanak, M. Shimoda, Y. Ishii, A. P. Tsai, and R. McGrath, Templated three-dimensional growth of quasicrystalline lead, *Nat. Commun.* **4**, 2715 (2013).
- [23] C. Cui, P. J. Nugent, M. Shimoda, J. Ledieu, V. Fournée, A. P. Tsai, R. McGrath, and H. R. Sharma, Structure of the twofold surface of the icosahedral Ag-In-Yb quasicrystal, *J. Phys.: Condens. Matter* **26**, 015001 (2013).
- [24] J. A. Smerdon, K. M. Young, M. Lowe, S. S. Hars, T. P. Yadav, D. Hesp, V. R. Dhanak, A. P. Tsai, H. R. Sharma, and R. McGrath, Templated quasicrystalline molecular ordering, *Nano Lett.* **14**, 1184 (2014).
- [25] C. Cui, M. Shimoda, and A. P. Tsai, Studies on icosahedral Ag-In-Yb: A prototype for Tsai-type quasicrystals, *RSC Adv.* **4**, 46907 (2014).
- [26] H. R. Sharma, P. J. Nugent, T. C. Q. Noakes, J. Smerdon, J. Parle, A. P. Tsai, and R. McGrath, Medium energy ion scattering (MEIS) study from the five-fold surface of icosahedral Ag-In-Yb quasicrystal, *J. Phys.: Conf. Ser.* **809**, 012017 (2017).
- [27] S. S. Hars, H. R. Sharma, J. A. Smerdon, S. Coates, K. Nozawa, A. P. Tsai, and R. McGrath, Growth of a bismuth thin film on the five-fold surface of the icosahedral Ag-In-Yb quasicrystal, *Surf. Sci.* **678**, 222 (2018).
- [28] S. Coates, S. Thorn, R. McGrath, H. R. Sharma, and A. P. Tsai, Unique growth mode observed in a Pb thin film on the threefold surface of an i-Ag-In-Yb quasicrystal, *Phys. Rev. Mater.* **4**, 026003 (2020).
- [29] D. Burnie, S. Coates, R. McGrath, and H. R. Sharma, Bias-voltage dependent STM images from the 2-fold surface of the icosahedral Ag-In-Yb quasicrystal, *J. Phys.: Conf. Ser.* **1458**, 012017 (2020).

- [30] F. Samavat, M. J. Gladys, C. J. Jenks, T. A. Lograsso, B. V. King, and D. J. O'Connor, Study of preferential sputtering and segregation effects on the surface composition of Al-Pd-Mn quasi-crystals, *Surf. Interface Anal.* **40**, 433 (2008).
- [31] G. Kresse and J. Furthmüller, Efficient iterative schemes for *ab initio* total-energy calculations using a plane-wave basis set, *Phys. Rev. B* **54**, 11169 (1996).
- [32] G. Kresse and D. Joubert, From ultrasoft pseudopotentials to the projector augmented-wave method, *Phys. Rev. B* **59**, 1758 (1999).
- [33] J. P. Perdew, K. Burke, and M. Ernzerhof, Generalized Gradient Approximation Made Simple, *Phys. Rev. Lett.* **77**, 3865 (1996).
- [34] J. Tersoff and D. R. Hamann, Theory of the scanning tunneling microscope, *Phys. Rev. B* **31**, 805 (1985).
- [35] K. Nozawa and Y. Ishii, Electronic structures and stability of Ag-In-Ca surfaces, *J. Phys.: Conf. Ser.* **226**, 012030 (2010).
- [36] Y. Ishii and T. Fujiwara, Hybridization Mechanism for Cohesion of Cd-Based Quasicrystals, *Phys. Rev. Lett.* **87**, 206408 (2001).
- [37] H. Euchner, T. Yamada, S. Rols, T. Ishimasa, Y. Kaneko, J. Ollivier, H. Schober, M. Mihalkovic, and M. de Boissieu, Tetrahedron dynamics in the icosahedral quasicrystals i-ZnMgSc and i-ZnAgSc and the cubic 1/1-approximant Zn₆Sc, *J. Phys.: Condens. Matter* **25**, 115405 (2013).
- [38] C. P. Gómez and S. Lidin, Comparative structural study of the disordered *MCd₆* quasicrystal approximants, *Phys. Rev. B* **68**, 024203 (2003).
- [39] K. Nishimoto, T. Sato, and R. Tamura, Low-temperature superstructures of a series of Cd₆-*M* (*M* = Ca, Y, Sr, Pr, Nd, Sm, Gd, Tb, Dy, Ho, Er, Tm, Yb and Lu) crystalline approximants, *J. Phys.: Condens. Matter* **25**, 235403 (2013).
- [40] P. Ebert, F. Yue, and K. Urban, Surface structures of cleaved icosahedral Al-Pd-Mn single quasicrystals after heat treatment, *Phys. Rev. B* **57**, 2821 (1998).